

## Microvibration analysis of a cantilever configured reaction wheel assembly

Zhe Zhang<sup>1a</sup>, Guglielmo S. Aglietti<sup>2b</sup>, Weijia Ren<sup>3c</sup> and Daniele Addari<sup>\*2</sup>

<sup>1</sup>University of Southampton, Southampton, Hampshire, SO17 1BJ, United Kingdom

<sup>2</sup>Surrey Space Centre, University of Surrey, Guildford, Surrey, GU2 7XH, United Kingdom

<sup>3</sup>Chinese Academy of Sciences, Beijing, 100094, People's Republic of China

(Received April 17, 2014, Revised May 7, 2014, Accepted May 8, 2014)

**Abstract.** This article discusses the microvibration analysis of a cantilever configured reaction wheel assembly. Disturbances induced by the reaction wheel assembly were measured using a previously designed platform. Modelling strategies for the effect of damping are presented. Sine-sweep tests are performed and a method is developed to model harmonic excitations based on the corresponding test results. The often ignored broadband noise is modelled by removing spikes identified in the raw signal including a method of identifying spikes from energy variation and band-stop filter design. The validation of the reaction wheel disturbance model with full excitations (harmonics and broadband noise) is presented and flaws due to missing broadband noise in conventional reaction wheel assembly microvibration analysis are discussed.

**Keywords:** microvibration; reaction wheel; disturbance model; broadband noise; cantilever configured

### 1. Introduction

In recent years satellite microvibrations and related issues have become increasingly important in the design of satellites carrying high-pointing accuracy instruments such as Hinode (Solar-B), GOCE, SDO and JWST. These satellites are equipped with highly vibration-sensitive instruments, resulting in stringent requirements for the satellite structure stability. Microvibrations are termed as low level mechanical disturbances usually in the range of micro-g's ( $\mu\text{g}$ ) typically occurring at frequencies from a few Hz up to 1 kHz (ECSS-E-HB-32-26A 2013). Microvibrations are usually generated by internal mechanisms on board satellites, such as Reaction Wheel Assemblies (RWAs), Momentum Wheel Assemblies (MWAs), cryocoolers, pointing mechanisms, thrusters, etc., which in this context are called disturbance sources (Zhang *et al.* 2009). The disturbances are caused by sources and transmitted through the spacecraft structure to the on-board instrumentation, here defined receivers, affecting its performance (Toyoshima *et al.* 2003). The dynamics of the microvibration sources will also couple with those of the satellite structure

---

\*Corresponding author, Ph.D. Student, E-mail: [d.addari@surrey.ac.uk](mailto:d.addari@surrey.ac.uk)

<sup>a</sup>Ph.D., E-mail: [zhezhang8311@gmail.com](mailto:zhezhang8311@gmail.com)

<sup>b</sup>Professor, E-mail: [g.aglietti@surrey.ac.uk](mailto:g.aglietti@surrey.ac.uk)

<sup>c</sup>Professor, E-mail: [renweijia@csu.ac.cn](mailto:renweijia@csu.ac.cn)

making the prediction of microvibration effects even more complicated (Takahara *et al.* 2004). From a practical standpoint, the reduction of the vibration level at a sensitive location of a structure can be attempted by action at the source(s), receiver(s) and along the vibration path(s). Passive damping technology and active control techniques are commonly used to achieve the desired performance (Aglietti *et al.* 2004, Tan *et al.* 2005).

The first step towards satellite microvibration analysis is to characterise the potential disturbance sources. Among the various sources on satellites, RWAs are often considered as one of the most important (Miller *et al.* 2007) and due to their complex dynamics, RWA microvibration characterisation is often difficult to perform. RWAs with the flywheel mounted symmetrically in the midst of a shaft supported by bearings on either side (mid-span configured RWAs) have been thoroughly studied in many papers. Early studies were mainly based on the general RWA disturbance test results and modelling for specific disturbance features (Bosgra and Prins 1982). Disturbances due to RWA components such as bearing, motor, flywheel (mass imbalances) etc., were carefully characterised from test results by Bialke (1992) and later modelled (Bialke 1996). RWA induced disturbances were modelled empirically assuming they consist of discrete harmonics superimposed with each other (Melody 1995). Most of the analyses on harmonic responses of a RWA were based on empirical modelling of disturbances due to each component (Laurens and Decoux 1997a, Laurens and Decoux 1997b). Analytical and empirical models of a RWA were developed also considering gyroscopic effects (Masterson *et al.* 2002, Masterson *et al.* 1999). Equations of Motion (EoMs) including flywheel mass imbalance were derived using energy methods and model parameter extractions were discussed in detail in similar works (Heimel 2011, Kim *et al.* 2010, Liu *et al.* 2008, Shin *et al.* 2010).

However, considering RWAs where the flywheel is mounted cantilever at one end of the shaft, disturbance models built for the typical symmetric mid-span configured RWAs are no longer valid, and hence new models need to be developed. On the other hand, due to ever increasing satellite stability requirements, broadband noise at mid and high frequencies has also become an important issue (ECSS-E-HB-32-26A 2013). Mechanical noise that exhibits smaller amplitudes compared to the main harmonics is therefore required to be included in the models, however there is a lack of appropriate methods to accurately model these types of microvibrations.

A broadband noise modelling method was introduced by Liu *et al.* (2008), and it was concluded that no purely analytical model was able to simulate broadband noise, thus it had to be modelled empirically. A hybrid broadband noise model was presented by Blaurock (2009), where an arbitrary broadband noise forcing function was realized as a speed dependent polynomial. This requires both an analytical “shape function” and test results at each speed. Apart from Blaurock (2009), there appear to be no other efforts that have attempted the modelling of RWA generated broadband noise for these applications.

A method to automatically identify spikes in the frequency spectrum (including harmonics and resonances) and accurately model higher harmonic excitations is introduced. This method allows the modelling of broadband noise with a simple and practical procedure and the quality of the simulation obtained using this mathematical model is validated by comparison against real test results.

## 2. RWA and mass imbalance disturbance model

### 2.1 Reaction wheel assembly

RWAs are high speed rotating mechanisms mainly used for satellite attitude control and slewing manoeuvres (Kenney 1963). A typical RWA consists of a rotating flywheel connected to a shaft suspended by mechanical bearings and driven by a brushless DC motor. A typical mechanical configuration of a RWA is “mid-span”, where the flywheel Centre of Mass (CoM) is located in the middle of the shaft with bearings at equal distance to the flywheel on each side; see Fig. 1(a). Alternatively, cantilever configured RWAs present the flywheel located at one end of the shaft with bearings on one side of the flywheel; see Fig. 1(a). In this paper, disturbances induced by a cantilever configured RWA are studied. In addition, a specially designed soft-suspension system is used to replace the traditional rigid support. The RWA, with its suspension system, was described by Zhou *et al.* (2011) and the schematic is presented in Fig. 1(b).

Generally speaking, disturbances generated by a typical RWA can be split into three categories based on their origin: ball bearing imperfections, motor imperfections and flywheel (static and dynamic) mass imbalances (Bialke 2011). At typical rotation speeds, flywheel mass imbalance disturbances are usually the highest ones. At some speeds the disturbances can be amplified by the RWA internal dynamics, i.e., RWA resonances. Mass imbalances generate disturbances at the same frequency of rotation of the flywheel fundamental harmonic (or H1). Irregularities in ball bearing, motor, lubrication etc., generate disturbances that usually occur at integral and/or fractional multiples of fundamental harmonic frequencies as sub- and super-harmonics (H0.5, H2, H2.7, H3 etc.) and their amplitudes are usually significantly smaller than those of fundamental harmonics.

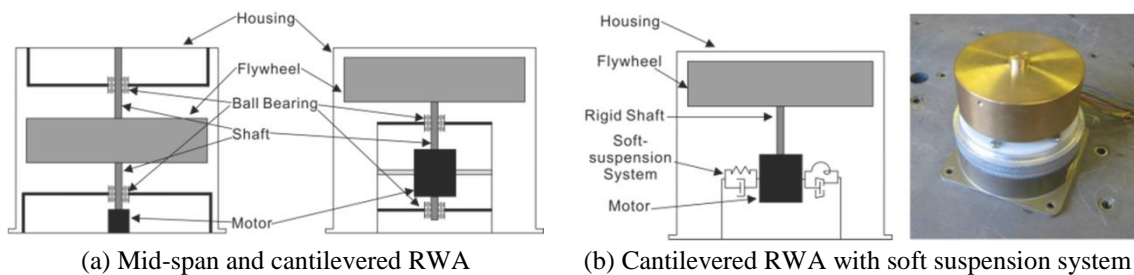


Fig. 1 RWA configuration

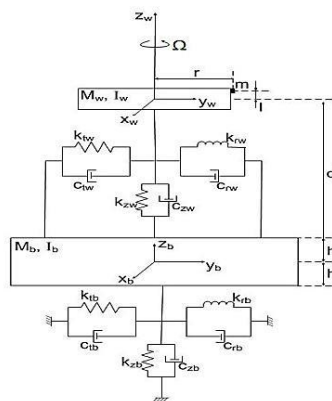


Fig. 2 Simplified RWA model

## 2.2 Mass imbalanced disturbance model

The mass imbalanced disturbance model of the cantilever configured RWA (referred as “RWA” for simplicity) was developed by Zhang *et al.* (2011) and subsequently re-elaborated to include the gyroscopic effect (Zhang *et al.* 2013). It is here briefly summarized for convenience of the readers. The RWA was simplified as the model shown in Fig. 2.

The RWA was assumed axisymmetric about its shaft pointing direction. The flywheel was modelled as a rigid disk with mass  $M_w$ , torsional inertia  $I_{Rw}$ , and polar inertia  $I_{Zw}$ . In addition, it is connected by a massless and rigid shaft of length  $d$  to the soft-suspension system. The inertial frame  $X_w Y_w Z_w$  and the body frame  $x_w y_w z_w$  coincided at the CoM of the flywheel  $O$  with  $z_w$ -axis (or  $Z_w$ -axis) defined in the shaft pointing direction. Rotations about the three axes in their corresponding frames are  $\theta_w$ ,  $\varphi_w$  and  $\psi_w$ . Let  $\Omega$  be the constant flywheel rotation speed and assume flywheel is at steady speed rotation,  $\Omega = \dot{\psi}_w$ . The wheel-base is modelled as a rigid disk of mass  $M_b$  and radial moment of inertia  $I_{Rb}$ . The dynamic mass imbalance can be model as a point mass  $m$ , placed at radius  $r$  on the flywheel and distance  $l$  from the shaft. Note that the amplitudes of the imbalance force are defined as the values proportional to the radial distance from the mass imbalance to the shaft axis. Although the radial distance and the flywheel radius are the same in Fig. 2, in practice, this radial distance has not to be the flywheel radius. The point mass creates radial forces and moments when the flywheel spins. The flexible components in this system are the soft-suspension system that connects the flywheel and the wheel-base (denoted with subscript “w”) and the soft-suspension system that connects the wheel-base to the ground (denoted with subscript “b”). The wheel-base-to-ground soft-suspension is able to represent the hard-mounted boundary condition when the spring stiffness values assume an infinite value and the “free-free” boundary condition when the spring stiffness values are considered zero.

The suspension system was modelled as a combination of five Degrees of Freedom (DoFs). This includes two combinations of linear spring and dashpot, two pairs of torsional spring and dashpot, each in one of the two radial translational DoFs ( $x$  and  $y$ ); a pair of linear spring and dashpot in the axial translational DoF ( $z$ ), see Fig. 2. Because of axisymmetry, the linear springs stiffness,  $k_{rw}$  and  $k_{rb}$ , are the same in the two radial translation DoFs, as well as the two torsional springs stiffness  $k_{rw}$  and  $k_{rb}$ , the two linear dashpot damping coefficients  $c_{rw}$  and  $c_{rb}$ , and the two torsional dashpot damping coefficients  $c_{rw}$  and  $c_{rb}$ . On the other hand, in the axial translation DoF,  $k_{zw}/k_{zb}$ , and  $c_{zw}/c_{zb}$ , represent the axial springs stiffness and the axial dashpot damping coefficients, respectively. The generalised Lagrangian coordinates in the WA model are ten:  $x_w$ ,  $y_w$ ,  $z_w$ ,  $\theta_w$ ,  $\varphi_w$ ,  $x_b$ ,  $y_b$ ,  $z_b$ ,  $\theta_b$  and  $\varphi_b$ , whereas  $\psi_w$  and  $\psi_b$  are not considered due to the assumption of flywheel steady speed rotation and, consequently, domination over angular speed perturbation in the torque DoF.

The mass imbalanced disturbance model was derived using an energy method (or Lagrangian approach) (Zhang *et al.* 2012a) and assuming infinite stiffness values for the suspension system which connects the wheel-base to the ground, i.e., representative of a hard-mounted boundary condition. Subsequently, only five DoFs of RWA are considered (Zhang *et al.* 2011).

Although the model captures RWA structural modes with gyroscopic effects, fundamental harmonics and their amplifications, it does not consider either sub- and super-harmonics or broadband noise. Harmonic model parameters are amplitude coefficients,  $C_i$  and harmonic numbers  $h_i$  for each harmonic. Since parameters are extracted from the corresponding harmonic disturbances at each DoF, phases between harmonics are assumed zero (or in-phase). Broadband noise is expressed as  $W_j(\Omega)$ , which is dependent on rotation speed at each DoF. Assuming all excitations are superimposed in the time domain at each DoF, the forcing vector can be expressed as

$$\begin{Bmatrix} F_x \\ M_y \\ F_y \\ M_x \\ F_z \end{Bmatrix} = \begin{Bmatrix} -\sum_{i=1}^{n_r} C_i^{rt} \Omega^2 \sin(h_i^{rt} \Omega t) + W_x(\Omega) \\ \sum_{i=1}^{n_{rr}} C_i^{rr} \Omega^2 \sin(h_i^{rr} \Omega t) + W_\varphi(\Omega) \\ \sum_{i=1}^{n_{rt}} C_i^{rt} \Omega^2 \cos(h_i^{rt} \Omega t) + W_y(\Omega) \\ \sum_{i=1}^{n_{rr}} C_i^{rr} \Omega^2 \cos(h_i^{rr} \Omega t) + W_\theta(\Omega) \\ \sum_{i=1}^{n_{at}} C_i^{at} \Omega^2 \sin(h_i^{at} \Omega t) + W_z(\Omega) \end{Bmatrix} \quad (1)$$

where superscripts *rt*, *rr* and *at* indicate radial translational, radial rotational and axial translational DoF respectively.  $W_j(\Omega)$  is the  $j^{\text{th}}$  DoF broadband noise excitation,  $n$  is the total number of harmonics in the model and  $i$  is the  $i^{\text{th}}$  harmonic considered in the model.

### 3. RWA disturbance tests

#### 3.1 Test description

A simple measurement platform was designed to measure RWA-induced disturbances in a hard-mounted boundary condition. Three independent test setups are required to retrieve the six disturbance forces and moments ( $F_x$ ,  $F_y$ ,  $F_z$ ,  $M_x$ ,  $M_y$  and  $M_z$ ). Detailed introductions of the platform and experimental setups are described by Zhang *et al.* (2012b).

In this study a cantilever configured RWA, 90 mm width, 90 mm height and 85 mm depth, (or 90×90×85 mm<sup>3</sup>) was adopted. The RWA consisted of a Brass-made rotor, an Aluminium 6082-made housing and a thermoplastic polymer-made suspension system, leading to a total mass of 1.5 kg. The rotor had a mass of 0.75 kg (including the DC motor) and a radial moment of inertia about the suspension system CoM,  $I_{rw}$ , of  $5.1 \times 10^{-4}$  kgm<sup>2</sup>. WA natural frequencies were retrieved from sine-sweep tests and discussed by Zhang *et al.* (2011).

The RWA was spun from 60 to 6000 rpm with a 60 rpm step increase and 5 s data were recorded at each speed. Force signals at each sensor were sampled at 2048 Hz with block size 2048, thus giving 1 Hz frequency resolution and 1 kHz useful frequency band (with anti-aliasing filter considered).

Disturbance tests were carried out in the Astronautics Dynamics Laboratory at the University of Southampton. For instance, the typical background noise for  $F_z$  (with power on) is plotted in Fig. 3(a) for example. It is also compared with typical RWA induced disturbances (soft and rigid suspensions) in Fig. 3(b).

The total Root Mean Square (RMS) value of  $F_z$  background noise in Fig. 3 a) is about 3.5 mN (10 Hz to 1 kHz). The contribution mainly comes from the spikes at 50 Hz and 150 Hz due to the UK power supply frequency. In practice they cannot be completely avoided although efforts were spent to reduce them, for example using some shielding. The two spikes appear throughout the test speed range with constant amplitudes, but they are much smaller compared to the harmonic responses, thus can be ignored.

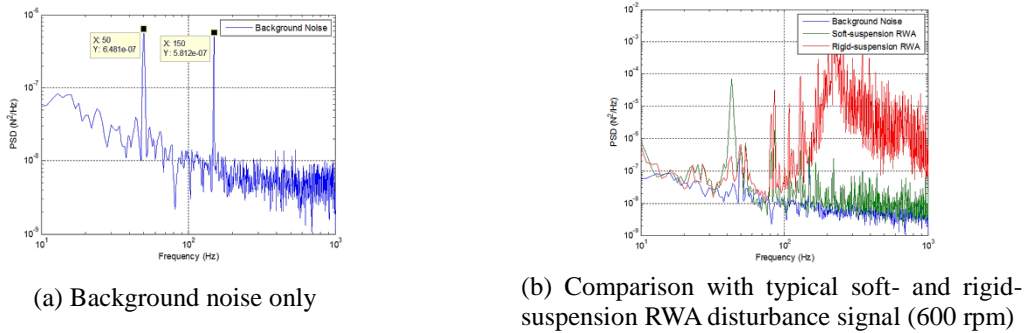


Fig. 3 Typical background noise of  $F_z$  (power on)

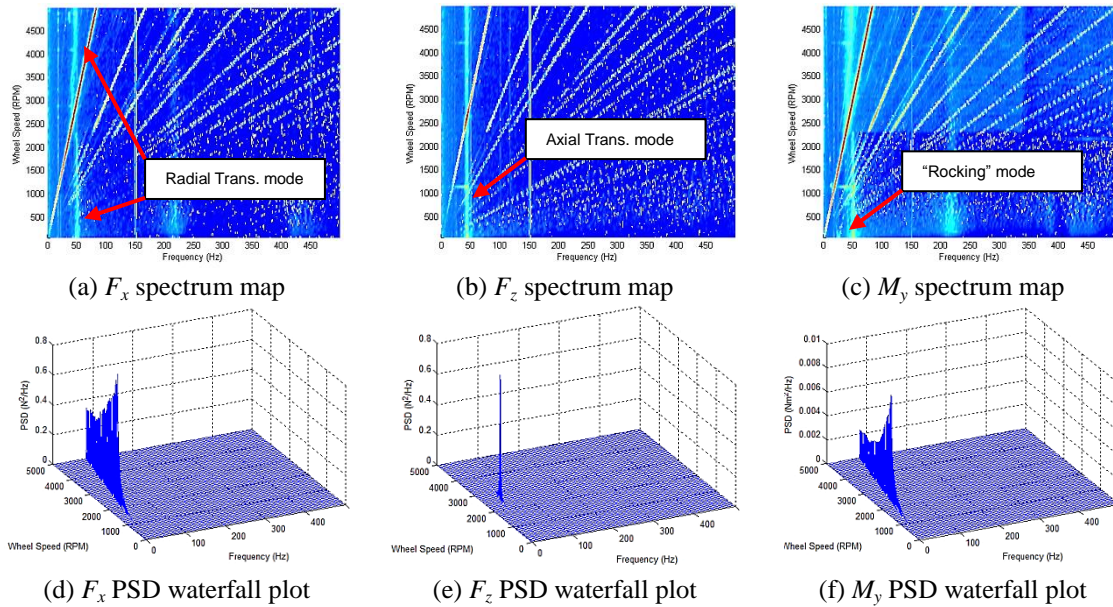


Fig. 4 Spectrum maps and PSD waterfall plots of selected DoFs

### 3.2 Test results

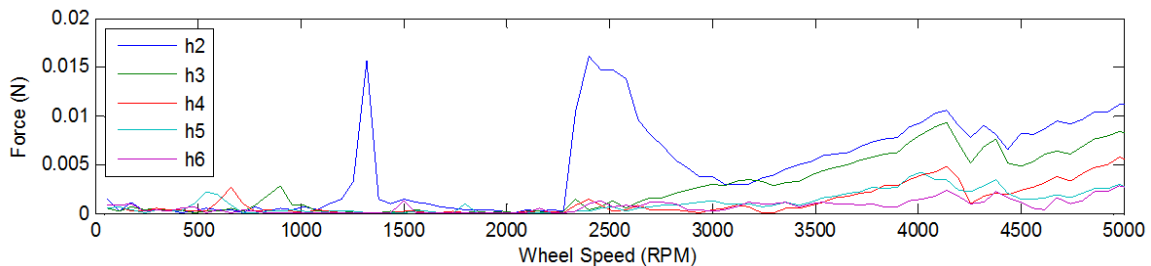
Fig. 4 presents spectrum maps and Power Spectral Density (PSD) waterfall plots for  $F_x$ ,  $F_z$  and  $M_y$ . The reader should note that, because of axisymmetry  $F_y$  and  $M_x$  assume similar values to  $F_x$  and  $M_y$ , respectively, and subsequently are not presented.

To improve results visibility in the spectrum maps, all disturbance amplitudes are scaled with  $10\log_{10}$  (amplitudes). The PSD waterfall plots are plotted in a linear scale and up to 5000 rpm.

Typical dynamic characteristics of a RWA are observed in Fig. 4. For example harmonic responses are clearly shown in spectrum maps in Fig. 4 (a)-(c). The red lines starting from the origin of the axes are fundamental harmonics and generate the highest responses. The other lines at different slopes are super- or higher harmonics (note no sub-harmonics appear in any case). It is also possible to see the other lines corresponding to the natural frequencies of RWA structural modes and also background noise (150 Hz line for example).

Table 1 Frequencies and amplitudes of primary resonances from disturbance tests

DoF	Frequency	Amplitude
$F_x$	41 Hz (or 2460 rpm)	1.36 N
$F_y$	40 Hz (or 2400 rpm)	1.34 N
$F_z$	44 Hz (or 2640 rpm)	1.36 N
$M_x$	40 Hz (or 2400 rpm)	0.135 Nm
$M_y$	41 Hz (or 2460 rpm)	0.136 Nm

Fig. 5 Higher harmonic responses of  $F_z$ 

The RWA structural modes are further discussed in Section IV. In the three PSD waterfall plots in Fig. 4 (d)-(f), only the fundamental harmonic responses can be seen. Since the soft-suspension system is used instead of a rigid design, higher harmonic responses have considerably smaller amplitudes than the fundamental harmonics.

From the practical point of view, they can be ignored in this RWA, but they are still modelled in this paper to complete the RWA disturbance model. In contrast, higher harmonics may be as equivalently important as fundamental harmonics in rigid design, for example in (Masterson *et al.* 1999).

As a further examination of  $F_x$  from the disturbance test results, Fig. 4(a) shows how higher harmonic responses are not obvious until 2280 rpm and then abruptly appear at high speeds indicating large amplitude changes.

Fundamental and higher harmonics were also extracted from the test results. Fundamental harmonic responses in radial DoFs (i.e.,  $x$  and  $y$ ) grow with the square of the speed before resonances. In contrast, a very sharp spike appears as resonance in the axial translational DoF (Zhang *et al.* 2012b). Frequencies and amplitudes of responses at resonances (i.e. the primary resonances) are listed in Table 1.

Responses of the first five integer higher harmonics (H2 to H6) of  $F_x$ ,  $M_y$  and  $F_z$  are also extracted from disturbance test results, for example  $F_z$  higher harmonic responses are presented in Fig. 5.

In Fig. 5 RWA structural modes are clearly visible. Moreover, other resonances can be observed. For instance, the spike at around 2500 rpm on H2 and resonances around 4300 rpm (i.e., a horizontal mode) can be noted. They are not considered in the disturbance modelling. Meanwhile, harmonic responses grow at much higher levels above the “separation speed” 2280 rpm compared to responses in the low speed region. These phenomena observed in higher harmonic responses are mainly due to nonlinearity. The extracted fundamental and higher harmonic responses are used for harmonic excitation modelling and disturbance model validation.

## 4. RWA disturbance model validation

### 4.1 Linear harmonic excitations modelling

Harmonic and broadband noise excitations act as inputs to the RWA disturbance model. In this section the modelling of the harmonic excitations and the validation of the structural modes are discussed.

The RWA structural modes are validated against test results. Campbell diagrams were obtained from the RWA mathematical model by assuming undamped free system, and therefore the classic eigenvalue problem was solved. The detailed process and results are discussed in (Zhang *et al.* 2012b).

The modelling process of the harmonic excitations includes two parts: identifying harmonics ( $h_i$ ) and estimating amplitude coefficients ( $C_i$ ). The estimation of  $C_i$  for each harmonic involves also estimating the speed power ( $n_i$ ). For simplicity, the first five integer harmonics ( $h_1$  to  $h_5$ ) are considered to demonstrate the modelling method. The method developed to estimate  $C_i$  is also introduced in this article.

In general, problems concerned with the estimation of  $C_i$  for the soft-suspension RWA are that:

- Flywheel mass imbalances are not exactly known, but only performance values from manufacture are given (typical static mass imbalance: < 5 g.mm).
- Fundamental harmonic responses severely interact with RWA structural modes in the test speed range, thus nonlinearity.
- Influences of dynamic amplifications must be considered.
- In practice, harmonic response amplitudes are not exactly proportional to the square of the spin speed (Seiler and Allegranza 2009).

In contrast for a conventional RWA design and the modelling methods developed in the past:

- Fundamental harmonic responses grow continuously and exponentially without any interaction in the test speed range.
- No dynamic amplifications are experienced in the test speed range.
- Harmonic responses are assumed proportional to the square of the spin speed.

Furthermore, these issues are all interrelated, thus making the modelling of harmonic excitations significantly more complicated than in the literature. Therefore, it is necessary to develop a method to efficiently and accurately simulate them. The method introduced here is a hybrid empirical and analytical method. The method is based on simulating the input harmonic parabola with its parameters obtained from the corresponding harmonic response test results. The overall modelling methodology is presented in Fig. 6.

The initial step is to find the spin speed, in this context defined “cut-off speed”, where dynamic amplifications are not yet influential in harmonic responses. Estimation of the “cut-off speed” is performed for fundamental harmonics only. The initial test values for the fundamental harmonic are the maximum mass imbalances (quoted by the RWA manufacturer) as amplitude coefficients (i) and power two (or squared) for the angular velocity (ii). The amplitude is estimated at each speed for each DoF (iii). This process is repeated up to the maximum speed for each DoF (iv). The corresponding test results are subsequently compared with simulated inputs for each DoF (v). A program was written to automatically adjust the amplitude coefficients and speed powers so that simulated harmonic amplitudes would match the test harmonic responses in all DoFs up to a the “cut-off speed” (vi).

As each DoF has a slightly different estimated “cut-off speed”, for the whole disturbance

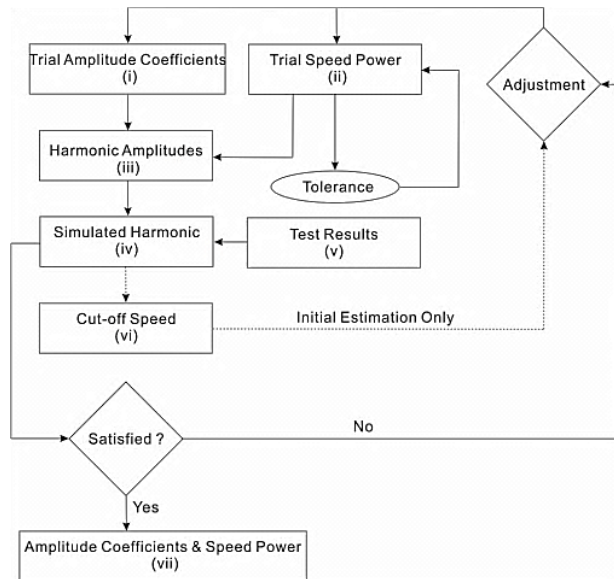
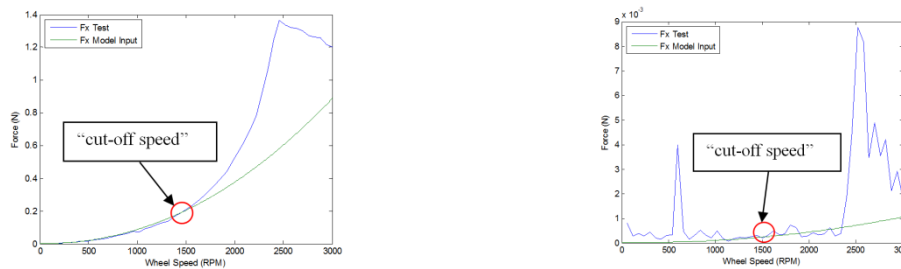


Fig. 6 Harmonic excitation modelling process



(a) Simulated H1 and estimated “cut-off speed”

(b) Simulated H5 with “cut-off speed” from H1

Fig. 7 Simulated  $F_x$  harmonic excitation with “cut-off speed”

modelling process the average value of DoFs is considered. The process of simulating fundamental harmonic amplitudes introduced here is repeated for other harmonics considered in the model (in this case  $H_2$  to  $H_5$ ) up to the “cut-off speed”. In other words, once the “cut-off speed” is found from fundamental harmonics, the simulation of any other harmonic is a trade-off process between amplitude coefficient and speed power to match simulated and test results up to the “cut-off speed”.

The trade-off process is carried out using the same program as in (vi). During the trade-off process, the speed power is checked with the defined tolerance (15% of power two). Results have shown the average value of  $v_c$  is about 1500 rpm. As an example, Fig. 7 presents the simulated fundamental harmonic and the fifth harmonic of  $F_x$ .

From Fig. 7, the simulated harmonic amplitudes match very well with the corresponding test harmonic responses at least up to the “cut-off speed”. Thereafter harmonic responses start being amplified by structural modes or resonances and the simulated harmonic amplitude continues growing with the estimated speed power. Similar results are also seen for other harmonics and DoFs.

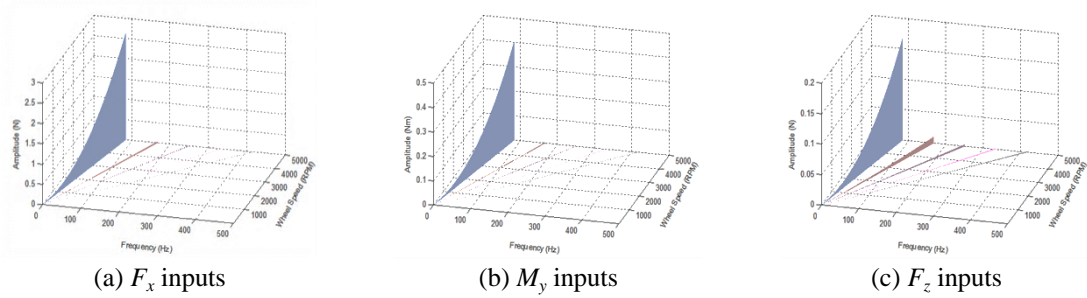


Fig. 8 Simulated harmonic excitations (H1 to H5)

Table 2 Amplitude coefficients and speed powers of simulated harmonic excitations

Harmonic Number	Amplitude Coefficient (kg m)	Speed Power	Amplitude Coefficient (kg m <sup>2</sup> )	Speed Power	Amplitude Coefficient (kg m)	Speed Power
	$F_x$		$M_y$		$F_z$	
H1	$4.5 \times 10^{-6}$		$3.26 \times 10^{-7}$		$1.35 \times 10^{-7}$	
H2	$4 \times 10^{-8}$		$1 \times 10^{-9}$		$8 \times 10^{-9}$	
H3	$1 \times 10^{-8}$		$3 \times 10^{-10}$		$2 \times 10^{-9}$	
H4	$5 \times 10^{-9}$	2.12	$1 \times 10^{-10}$	2.25	$1 \times 10^{-9}$	2.24
H5	$4 \times 10^{-9}$		$2 \times 10^{-10}$		$8 \times 10^{-10}$	

Simulated harmonic excitations of  $F_x$ ,  $M_y$  and  $F_z$  are shown in amplitude waterfall plots in Fig. 8. As a matter of fact higher harmonics have much smaller amplitudes compared to fundamental harmonics, especially for high order harmonics.

The final amplitude coefficients ( $C_i$ ) and speed powers ( $n_i$ ) of simulated harmonic excitations are listed in Table 2.

#### 4.2 Linear harmonic responses simulation

Harmonic responses are simulated using the state space method. Generally, a dynamic system can be expressed as

$$M\ddot{x}(t) + C\dot{x}(t) + Kx(t) = Q(t) \tag{2}$$

where  $M$ ,  $C$  and  $K$  are mass matrix, damping matrix and stiffness matrix respectively.  $x(t)$  is the response displacement vector and  $Q(t)$  is the input or excitation vector. If the system is linear, its state space form can be derived. Let  $x_1(t)=x(t)$  and  $x_2(t)=\dot{x}(t)$ , (2) then becomes:

$$\begin{Bmatrix} \dot{x}_1(t) \\ \dot{x}_2(t) \end{Bmatrix} = \begin{bmatrix} 0 & I \\ -M^{-1}K & -M^{-1}C \end{bmatrix} \begin{Bmatrix} x_1(t) \\ x_2(t) \end{Bmatrix} + \begin{bmatrix} 0 \\ M^{-1} \end{bmatrix} Q(t) \tag{3}$$

$$x(t) = \begin{bmatrix} I & 0 \end{bmatrix} \begin{Bmatrix} x_1(t) \\ x_2(t) \end{Bmatrix} \tag{4}$$

Harmonic responses are simulated for the two conditions based on the suspension system

Table 3 RWA damping at static for disturbance modelling

Mode	Damping Ratio		Damping Value	
Translational	$\zeta_r$	0.15	$c_{rw}$	68.2 kg/s
Rocking	$\zeta_r$	0.15	$c_{rw}$	0.026 kg m <sup>2</sup> /s/rad
Axial	$\zeta_z$	0.02	$c_{zw}$	8.3 kg/s

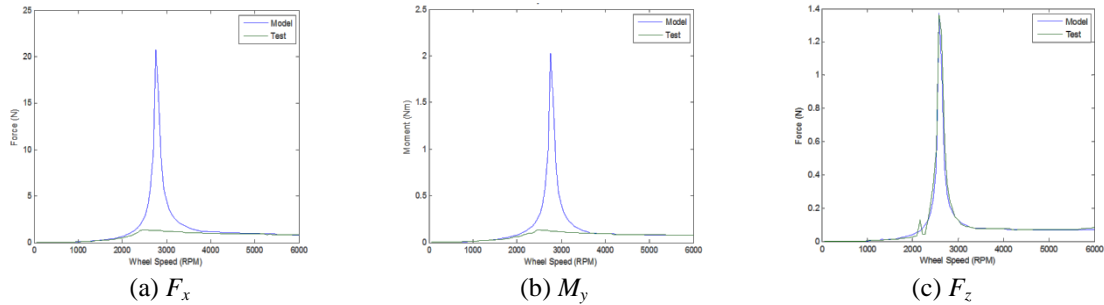


Fig. 9 Simulated H1 responses compared with test results (low level damping)

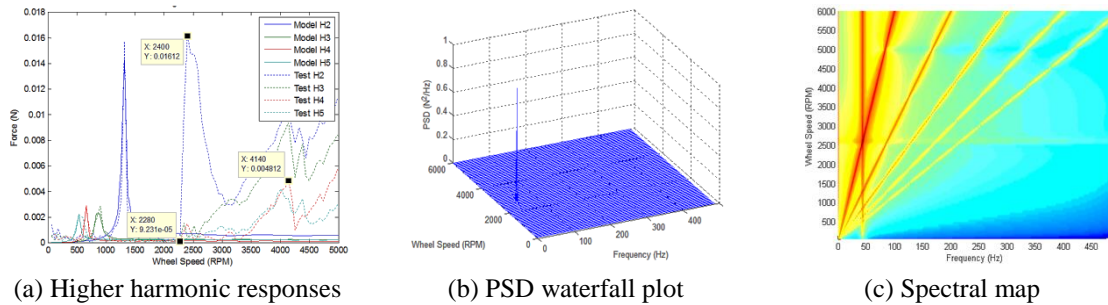


Fig. 10 Simulated  $F_z$  harmonic response

damping, i.e., damping values from low level sine-sweep test and high level sine-sweep test. Damping ratios have been extracted from disturbance test results, with the RWA reference FE model, and the resulting damping values are listed in Table 3.

Recalling from disturbance test results, RWA induced disturbances exhibit low damping characteristics in  $F_z$  but highly damped radial DoFs in  $F_x$ ,  $F_y$ ,  $M_x$  and  $M_y$ . Therefore it is expected that the disturbance model with low level damping ratios ( $\zeta=0.02$ ) is not appropriate to simulate the dynamics in radial DoFs. Subsequently, high level damping ratios ( $\zeta=0.15$ ) are adopted in the disturbance model. In this way, a systematic approach of modelling damping values and disturbances can be formulated. Simulated fundamental harmonics with low level damping ratios are presented in Fig. 9.

In Fig. 9(c), simulated responses and test results match well in  $F_z$  at all frequencies. In contrast in  $F_x$  and  $M_y$  in Fig. 9 (a)-(b), the disturbance model with low level damping ratios could not simulate the highly damped resonant amplitudes in radial DoFs, but results are well matched at other frequencies.

Simulated higher harmonic responses of  $F_z$  are presented in Fig. 10(a). They are also plotted as PSD waterfall plot and spectral maps in Fig. 10 (b)-(c) respectively.

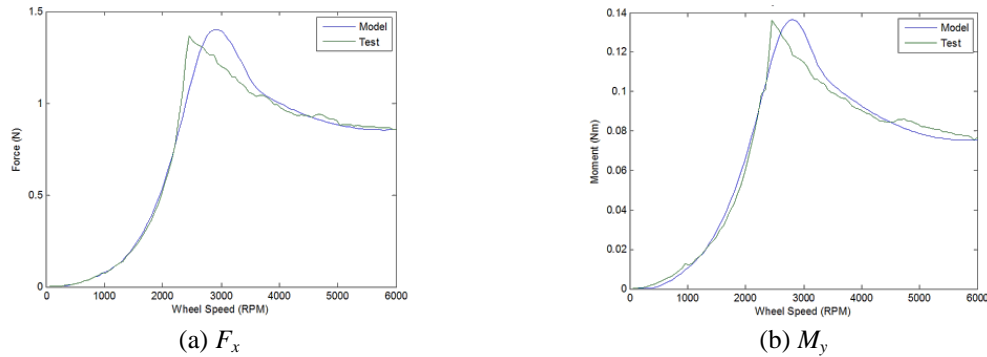
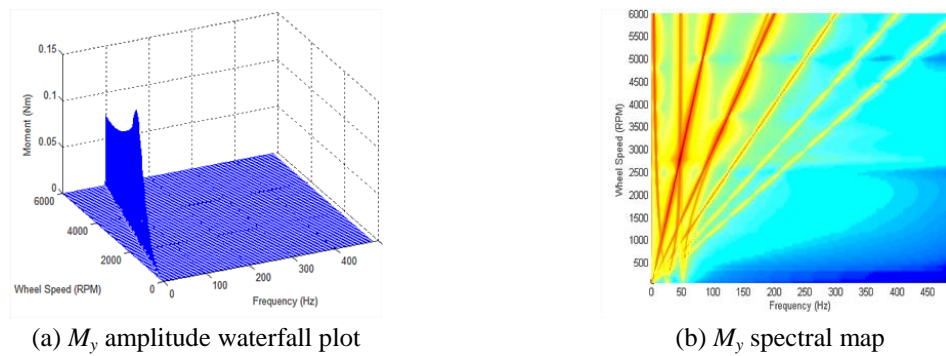


Fig. 11 Simulated H1 responses compared with test results (high damping value)

Fig. 12 Simulated  $M_y$  harmonic response

In Fig. 10(a), the disturbance model with low level damping has accurately captured harmonic responses and resonances below 2280 rpm. Disturbances above this speed and resonances not considered in the disturbance model, such as resonances at 2400 rpm and 4140 rpm, could not be simulated. The simulated higher harmonic amplitudes are too small to be seen in the waterfall plot in a linear scale as expected but are revealed in spectral map.

Higher harmonics in radial DoFs are not presented here but they are simulated using the same method and they have shown similar characteristics as in Fig. 10(a).

Simulated fundamental harmonic responses with high level damping ratio are presented in Fig. 11.

In Fig. 11, resonant amplitudes of simulated fundamental harmonic responses are better matched with the test results compared to the previous cases shown in Fig. 9. The slight disparity (360 rpm or 6 Hz) between simulated and test resonance is still under investigation. Besides this, fundamental harmonic responses have been accurately simulated in radial DoFs.

In Fig. 12 an example of simulated disturbances in radial rotational DoF are plotted as amplitude waterfall plots and spectral maps.

To summarise, in order to be consistent with the test data the model implements different values of damping about the axial DoF and the radial DoF. The responses along the axial DoF and the radial DoF are shown in Fig. 9(c) and Fig. 11, respectively.

Simulated frequencies and amplitudes of responses at resonances (i.e., the primary resonances) are compared with test results and listed in Table 4.

Table 4 Frequencies and amplitudes of primary resonances from simulation

DoF	Model		Test	
	Frequency	Amplitude	Frequency	Amplitude
$F_x$	47 Hz (or 2820 rpm)	1.39 N	41 Hz (or 2460 rpm)	1.36 N
$F_y$	47 Hz (or 2820 rpm)	1.39 N	40 Hz (or 2400 rpm)	1.34 N
$F_z$	44 Hz (or 2640 rpm)	1.36 N	44 Hz (or 2640 rpm)	1.36 N
$M_x$	47 Hz (or 2820 rpm)	0.137 Nm	40 Hz (or 2400 rpm)	0.135 Nm
$M_y$	47 Hz (or 2820 rpm)	0.137 Nm	41 Hz (or 2460 rpm)	0.136 Nm

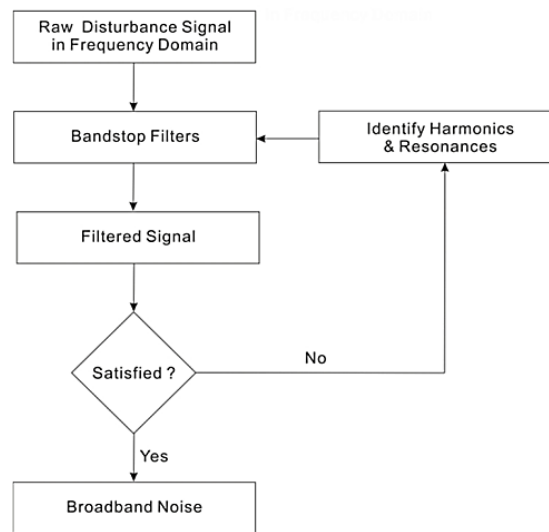


Fig. 13 Broadband noise modelling process

## 5. Broadband noise model development

### 5.1 Introduction

Generally, in the frequency spectrum amplitudes of broadband noise are notably smaller compared to those of specific harmonic response spikes. The broadband noise modelling method developed in this article is an empirical method that utilizes a number of band-stop filters in order to block the identified spikes (include any harmonic and resonance), hence the remaining noise in the disturbance signal is broadband noise; such a signal is used as the broadband noise model. The modelling process of broadband noise at any spin speed can be illustrated in Fig. 13.

### 5.2 Spikes identification

Distinct spikes in a disturbance signal such as harmonics and resonances must be identified first. In this article, the method is based on the cumulative RMS (already defined in Section 3.1, last paragraph, pg. 7) value plot of a disturbance signal. For example, a PSD and cumulative RMS value plot of  $F_z$  at 1800 rpm is used to demonstrate the broadband noise modelling and later the full disturbance model validation; these are shown in Fig. 14 respectively.

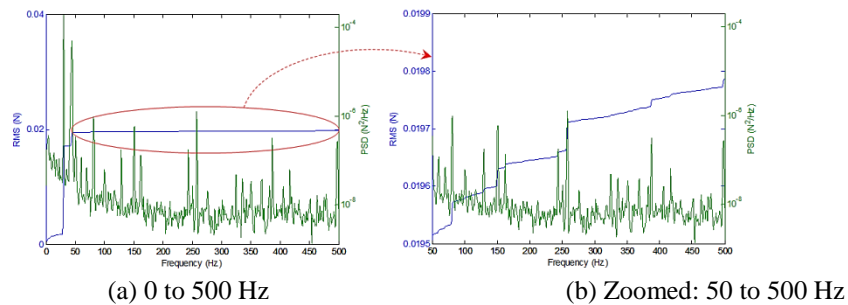
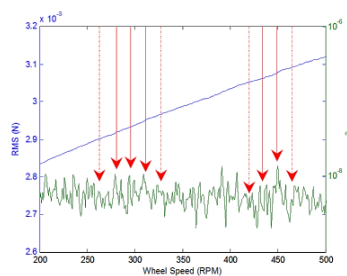
Fig. 14 PSD and cumulative RMS value plot of  $F_z$  (1800 rpm)

Fig. 15 PSD and cumulative RMS of background noise (200 Hz to 500 Hz)

Generally, in a typical cumulative RMS value plot a step change at a frequency indicates a spike with distinctive amplitude and this amount of energy is contributed to the signal. The distinctive spike could be either harmonic or resonance. The RMS value at the maximum frequency is the total energy accumulated in the signal at that speed.

The cumulative RMS value plot is particularly useful for broadband noise modelling, since all distinctive spikes (regardless of harmonics or resonances) that fall within the defined criteria (e.g., a critical RMS value, discussed later) can be easily identified in the signal.

For soft-suspended RWA, broadband noise and background noise are also similar regardless of the speed, particularly in the high frequency band; see Fig. 3(b) as an example. The critical RMS value is obtained from the RMS values of two neighbouring spikes in the background noise. Fig. 15 shows a segment (between 200 to 500 Hz) PSD and cumulative RMS plots of the background noise.

In Fig. 15, it is found that distinctive spikes appear approximately every 20 Hz. These spikes have similar amplitudes, thus the cumulative RMS value grows smoothly without distinct steps, see also the blue line in Fig. 15. These spikes in the background noise are similar to those at high frequencies in the broadband noise when the RWA spins. Due to this reason, the RMS value difference of every two neighbouring spikes in the frequency band in the background noise is calculated and their average value is used as the critical RMS value for identifying spikes in disturbance signal at any speed. In this case, the critical RMS value is estimated to be about  $1.5 \times 10^{-5}$  N.

Using this method, steps with RMS value difference exceeding the critical RMS value in the cumulative RMS plot of a disturbance signal (such as in Fig. 14(b)) are identified. These identified steps correspond to the spikes which need to be removed from the signal. In fact, this method is accurate enough to identify and remove all harmonics, resonances and also some other distinctive

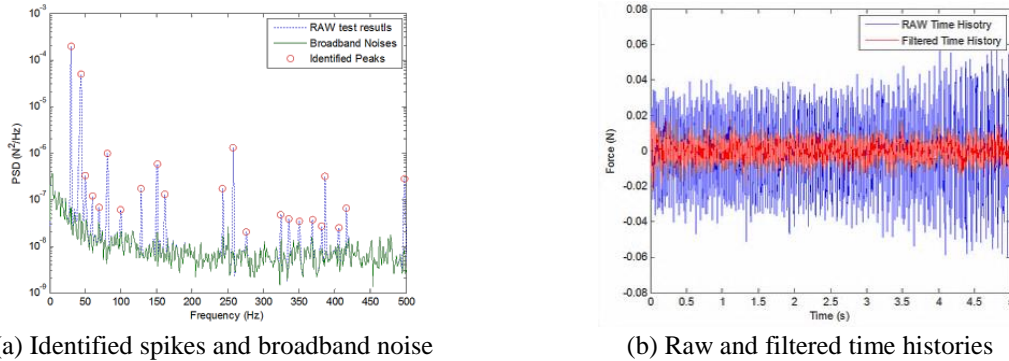


Fig. 16 Example of identified spikes and broadband noise model ( $F_z$  at 1800 rpm)

Table 5 Parameters of the band-stop filter to remove spike at 258 Hz

Parameters	Values
Pass-band corner frequency	257.9 Hz
Stop-band corner frequency	258.1 Hz
Pass-band ripple	1
Stop-band attenuation	3
The lowest order	1
Normalized cut-off frequency band	[257.5 258.5] Hz

spikes in the noise. For example, identified spikes of  $F_z$  at 1800 rpm in the frequency band of interest (0 to 500 Hz) are shown in Fig. 16(a) plotted as red circles.

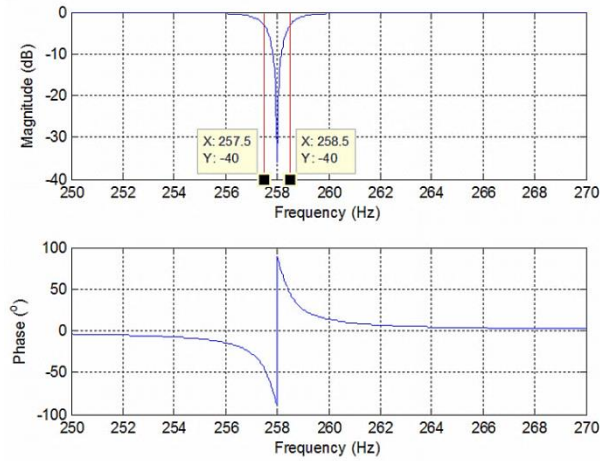
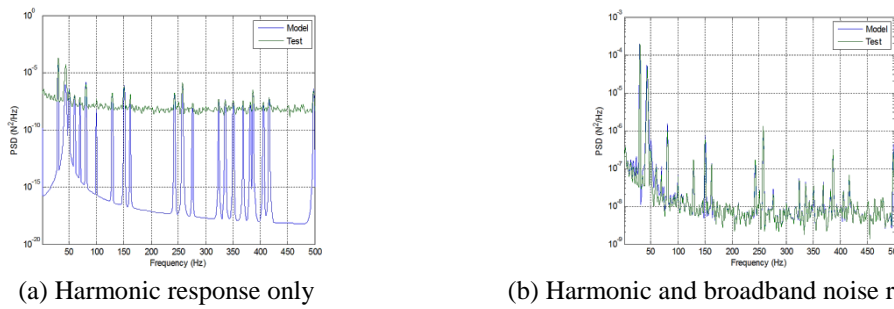
### 5.3 Band-stop filtering

Typical Butterworth band-stop filters are adopted to remove the identified spikes. Because each identified spike needs a band-stop filter to remove it, characteristics of bandstop filters depend on the frequency of each spike and the universal filter parameters. For instance, parameters of the filter to remove the spike at 258 Hz are given in Table 5.

The resulting magnitude and phase of this filter are plotted in Fig. 17.

The band-stop filter has been designed with a narrow cut-off frequency band (in this case  $\pm 0.5$  Hz for every spike) removing only the identified spike hence minimizing influences to the surrounding signals. The reducing magnitude at each identified frequency is designed for -36 dB for every spike so that the amplitude changes at identified spikes do not overshoot the general broadband noise level. On the other hand, this reduction level is large enough to remove some spikes with small amplitudes at once (e.g., 100 Hz and 276 Hz) but only partially reduce large spike amplitudes (e.g., 30 Hz and 44 Hz). Therefore an iteration process of spike identification and filtering is programmed to completely remove them.

The final filtered  $F_z$  disturbances at 1800 rpm are plotted in both the frequency domain (Fig. 16(a)) and the time domain (Fig. 16(b)) and are also compared with the corresponding raw disturbances. In the frequency domain, it is clear that identified spikes have been removed and amplitudes are close to neighbouring signals, i.e., broadband noise. In the time domain, broadband noise amplitudes remain at almost the same level in the entire frequency band as expected.

Fig. 17 Band-stop filter example ( $F_z$  at 1800 rpm, 258 Hz spike)

(a) Harmonic response only

(b) Harmonic and broadband noise responses

Fig. 18 Simulated responses of  $F_z$  at 1800 rpm with and without broadband noise

Since broadband noise at each speed is similar for the soft-suspended RWA presented in this article, the broadband noise obtained at any speed is accepted as the universal broadband noise, i.e., they are speed independent. Consequently, the universal broadband noise model can be superimposed with harmonic excitations at any speed to simulate the full excitation at that speed for each DoF. The method can also be used for conventional RWA broadband noise modelling. In case it becomes speed dependent due to possible broadband amplifications at high frequencies such as in Fig. 3(b), a speed dependent shape function is required and it could be obtained either empirically or analytically.

#### 5.4 Full disturbance model validation

RWA full disturbance model includes harmonic and broadband noise excitations allowing their responses to be predicted with also the consideration of RWA structural modes and gyroscopic effects. All excitations are superimposed in the time domain for each DoF and used as inputs in the model.

Responses of  $F_z$  at 1800 rpm considering only harmonic excitations are predicted and compared with the corresponding test results; see Fig. 18(a) as an example. Subsequently, the full excitation (harmonic and broadband noise) is applied and responses are presented in Fig. 18(b). All curves

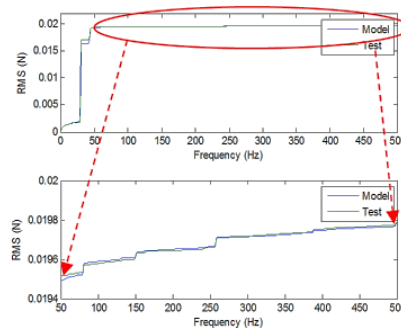


Fig. 19 RMS values of simulated and test results ( $F_z$  at 1800 rpm)

are plotted in a PSD logarithmic scale.

Fig. 18(a) shows the simulated harmonic responses without considering broadband noise. They assume the typical disturbance form as those predicted using other modelling methods in the literature. Although harmonic responses and resonances have been correctly modelled in Fig. 18(a), it is clear that at other broadband frequencies the simulated curve remains at much lower response level i.e., they are unexcited. The general response level is mainly influenced by the RWA structural mode, in this case the radial translational mode at 44 Hz only in  $F_z$ . It is worth mentioning that all these flaws in the disturbance model derived from not considering broadband noise are not obvious in a liner scale, but clearly revealed in logarithmic scale. On the other hand, since energy in the signal is mainly contributed from harmonic responses and resonant amplifications, the traditional RWA disturbance models are still accurate to a certain extent.

Fig. 18(b) shows the predicted responses from the RWA disturbance model considering all excitations. In this case the complete frequency band has been excited and the simulated results precisely match the test results. Although harmonic responses and resonant amplitudes have slightly increased due to the additional broadband noise, their absolute amplitudes remain significantly smaller compared to harmonic responses and resonant amplitudes, subsequently they have very little influence but they significantly elevate the regions that have not been previously excited.

Cumulative RMS values of simulated responses are calculated and plotted in Fig. 19 with test results. The detailed representation of curves between 50 and 500 Hz after the primary resonance (1800 rpm or 30 Hz) is also plotted in the figure.

Fig. 19 provides qualitative comparisons between simulated and test results at all frequencies. From the figure it is clear that RMS or energy curves are closely matched across the entire frequency band, especially at high frequencies (after the primary resonance or 30 Hz) where broadband noise has most influence.

## 6. Conclusions

In this article, a methodology for modelling the mechanical disturbances produced by a Cantilever Configured Reaction Wheel Assembly has been presented and validated against test results. Due to the cantilever configuration, the dynamics along the radial DoFs are coupled between each other and the traditional models based on symmetric designs are not valid anymore.

In this article, the coupled RWA disturbance model is solved numerically using the state space approach. A method is developed to model linear harmonic excitations. This method is based on the empirical modelling of harmonic responses up to the speeds where the dynamic amplification due to resonance is not influential. Linear harmonic responses are simulated in the time domain. In the disturbance model, low and high level damping values are used for axial translational DoF and radial DoFs respectively and results have shown good agreement between simulated and test results for each case. A method is also introduced to model the traditionally ignored broadband noise. Band-stop filters are designed to remove the identified spikes (using energy method or a cumulative RMS plot) in the disturbance signal, with the remaining being broadband noise. Also the full RWA disturbance model is validated against test results by considering harmonic responses and broadband noises. The excellent level of correlation between test results and model predictions confirms that the methods developed in this article can accurately simulate the cantilevered RWA-induced disturbances.

In conclusion, the microvibration study discussed in this article presents a modelling method which is programmed to perform RWA microvibration analysis automatically, systematically and efficiently and it can be applied to the conventional (and also relatively simpler) designs such as symmetrical mid-span configured RWAs.

## Acknowledgements

The author would like to thank SSBV UK for their support.

## References

- Aglietti, G.S., Langley, R.S., Rogers, E. and Gabriel, S.B. (2004), "Model building and verification for active control of microvibrations with probabilistic assessment of the effects of uncertainties", *Proceedings of the Institution of Mechanical Engineers, Part C: Journal of Mechanical Engineering Science*, **218**(4), 389-399.
- Bialke, B. (2011), "Microvibration disturbance fundamentals for rotating mechanisms", *Proceedings of the 34th Annual Guidance and Control Conference*, Breckenridge, CO.
- Bialke, B. (1996), "Microvibration disturbance sources in reaction wheels and momentum wheels", *Proceedings of the European Conference on Spacecraft Structures, Materials & Mechanical Testing*, Noordwijk, The Netherlands.
- Bialke, B. (1992), "A new family of low cost momentum/reaction wheels", *Proceedings of the Annual AAS Guidance and Control Conference*, Keystone, CO.
- Bosgra, J. and Prins, J.J.M. (1982), "Testing and investigation of reaction wheels", *Proceedings of the Automatic Control in Space, 9th Symposium*.
- ECSS-E-HB-32-26A, ECSS-E-HB-32-26A Spacecraft Mechanical Loads Analysis Handbook, ESA Requirements and Standards Division, ESA Requirements and Standards Division.
- Heimel, H. (2011), "Spacewheel microvibration - sources, appearance, countermeasures", *Proceedings of the 8th Int'l ESA Conference on Guidance & Navigation Control Systems*, Karlovy Vary, Czech Republic
- Kenney, H.B. (1963), "A Gryo momentum exchange device for space vehicle attitude control", *AIAA J.*, **1**(5), 1110-1118.
- Kim, D.K., Oh, S.H., Yong, K.L. and Yang, K.H. (2010), "Numerical study on a reaction wheel and wheel-disturbance modeling", *J. Korean Soc. Aeronaut. Space Sci.*, **38**(7), 702-708.
- Laurens, P. and Decoux, E. (1997a), "Microdynamic behaviour of momentum and reaction wheels",

- Proceedings of the Second Space Microdynamics and Accurate Symposium*, Toulouse, France.
- Laurens, P. and Decoux, E. (1997b), "Understanding and monitoring space mechanisms through their microdynamic signature", *Proceedings of the 7th European Space Mechanisms and Tribology Symposium*, Noordwijk, Netherlands.
- Liu, K.C., Maghami, P. and Blaurock, C. (2008), "Reaction wheel disturbance modeling, jitter analysis, and validation tests for solar dynamics observatory", *Proceedings of the AIAA Guidance, Navigation and Control Conference and Exhibit*, Honolulu, Hawaii.
- Masterson, R.A., Miller, D.W. and Grogan, R.L. (2002), "Development and validation of reaction wheel disturbance models: empirical model", *J. Sound Vib.*, **249**(3), 575-598.
- Masterson, R.A., Miller, D.W. and Grogan, R.L. (1999), "Development of empirical and analytical reaction wheel disturbance models", *Proceedings of the Structures, Structural Dynamics and Materials Conference*, St. Louis, MO, USA.
- Miller, S.E., Kirchman, P. and Sudey, J. (2007), "Reaction wheel operational impacts on the GOES-N jitter environment", *Proceedings of the AIAA Guidance, Navigation and Control Conference and Exhibit*, South Carolina, USA.
- Seiler, R. and Allegranza, C. (2009), "Mechanism noise signatures: identification and modelling", *Proceedings of the 14th European Space Mechanisms and Tribology Symposium*, Vienna, Austria.
- Shin, Y.H., Heo, Y.H., Oh, S.H., Kim, D.K., Kim, K.J. and Yong, K.L. (2010), "Identification of input force for reaction wheel of satellite by measured action force on decelerating", *Tran. Korean Soc. Noise Vib. Eng.*, **20**(3), 263-271.
- Takahara, O., Yoshida, N. and Minesugi, K. (2004), "Microvibration transmissibility test of solar-B", *Proceedings of the 24th International Symposium on Space Technology and Science*, Miyazaki, Japan
- Tan, A., Meurers, T., Veres, S., Aglietti, G. and Rogers, E. (2005), "Robust control of microvibrations with experimental verification", *Proceedings of the Institution of Mechanical Engineers, Part C: Journal of Mechanical Engineering Science*, **219**(5), 453-460.
- Toyoshima, M., Jono, T., Takahashi, N., Yamawaki, T., Nakagawa, K. and Arai, K. (2003), "Transfer functions of microvibrational disturbances on a satellite", *Proceedings of the 21st International Communications Satellite Systems Conference and Exhibit*, Yokohama, Japan
- Zhang, Z., Aglietti, G. and Ren, W. (2012a), "Microvibration model development and validation of a cantilevered reaction wheel assembly", *Appl. Mech. Mater.*, **226-228**, 133-137.
- Zhang, Z., Aglietti, G. and Zhou, W. (2011), "Microvibrations induced by a cantilevered wheel assembly with a soft-suspension system", *AIAA J.*, **49**(5), 1067-1079.
- Zhang, Z., Ren, W. and Aglietti, G. (2012b), "Coupled disturbance modelling and validation of a reaction wheel model", *Proceedings of the European Conference on Spacecraft Structures, Materials & Environmental Testing*, Noordwijk, The Netherlands.
- Zhang, Z., Aglietti, G.S. and Ren, W. (2013), "Coupled microvibration analysis of a reaction wheel assembly including gyroscopic effects in its acceleration", *J. Sound Vib.*, **332**(22), 5748-5765.
- Zhang, Z., Yang, L. and Pang, S. (2009), "Jitter environment analysis for micro-precision spacecraft", *Spacecraft Environ. Eng.*, **26**(6), 528-534.
- Zhou, W.Y., Aglietti, G.S. and Zhang, Z. (2011), "Modelling and testing of a soft suspension design for a reaction/momentum wheel assembly", *J. Sound Vib.*, **330**(18-19), 4596-4610.

EC

## Nomenclature

$C$	=	amplitude coefficient
$\mathbf{C}$	=	damping matrix

$c$	=	dashpot damping coefficient
$d$	=	shaft length
$f$	=	natural frequency
$F$	=	force
$h$	=	wheel-base half height/harmonic number
$\mathbf{I}$	=	inertia tensor
$I_r$	=	transverse moment of inertia
$k$	=	spring stiffness
$\mathbf{K}$	=	stiffness matrix
$L$	=	flywheel half height
$M$	=	mass/moment
$\mathbf{M}$	=	mass matrix
$m$	=	imbalance mass
$n$	=	number of harmonics/speed power
$O$	=	centre of mass
$\mathbf{Q}$	=	input or excitation vector
$r$	=	radial distance from flywheel centre of mass to imbalance mass
$t$	=	time
$v$	=	velocity
$W$	=	broadband noise
$\mathbf{x}$	=	displacement response vector
$X, Y, Z$	=	displacement in inertial frame
$\theta, \varphi, \psi$	=	rotations about the three orthogonal axes x, y and z respectively
$\zeta$	=	damping ratio
$\Omega$	=	flywheel rotation speed

*Sub- and super- scripts*

$at$	=	axial translational DoF
$i$	=	the number of harmonics
$r$	=	torsional (spring and dashpot)
$rt$	=	radial translational DoF
$rr$	=	radial rotational DoF
$t$	=	linear (spring and dashpot)
$w$	=	reaction wheel assembly
$x, y, z$	=	in the three translational DoFs, respectively
$R$	=	total radial (damping)
$\theta, \varphi, \psi$	=	in the three rotational DoFs, respectively